ARTICLE

Check for updates

Metal 3D printing technology for functional integration of catalytic system

Qinhong Wei[1,2,7], Hangjie Li[1,7], Guoguo Liu[1,7], Yingluo He[1], Yang Wang[1], Yen Ee Tan[1], Ding Wang[3], Xiaobo Peng [4,5✉], Guohui Yang [1,6✉] & Noritatsu Tsubaki [1✉]

Mechanical properties and geometries of printed products have been extensively studied in metal 3D printing. However, chemical properties and catalytic functions, introduced by metal 3D printing itself, are rarely mentioned. Here we show that metal 3D printing products themselves can simultaneously serve as chemical reactors and catalysts (denoted as self-catalytic reactor or SCR) for direct conversion of C1 molecules (including CO, CO_2 and CH_4) into high value-added chemicals. The Fe-SCR and Co-SCR successfully catalyze synthesis of liquid fuel from Fischer-Tropsch synthesis and CO_2 hydrogenation; the Ni-SCR efficiently produces syngas (CO/H_2) by CO_2 reforming of CH_4. Further, the Co-SCR geometrical studies indicate that metal 3D printing itself can establish multiple control functions to tune the catalytic product distribution. The present work provides a simple and low-cost manufacturing method to realize functional integration of catalyst and reactor, and will facilitate the developments of chemical synthesis and 3D printing technology.

[1] Department of Applied Chemistry, School of Engineering, University of Toyama, Gofuku 3190, Toyama 930-8555, Japan. [2] Department of Chemical Engineering, School of Petrochemical Technology and Energy Engineering, Zhejiang Ocean University, Zhoushan 316022, China. [3] School of Material Science & Engineering, University of Shanghai for Science and Technology, Shanghai 200093, China. [4] National Institute for Materials Science, 1-1 Namiki, Tsukuba, Ibaraki 305-0044, Japan. [5] Key Laboratory of the Ministry of Education for Advanced Catalysis Materials, Institute of Physical Chemistry, Zhejiang Normal University, Jinhua 321004, China. [6] State Key Laboratory of Coal Conversion, Institute of Coal Chemistry, Chinese Academy of Sciences, Taiyuan 030001, China. [7] These authors contributed equally: Qinhong Wei, Hangjie Li, Guoguo Liu. ✉email: PENG.Xiaobo@nims.go.jp; thomas@eng.u-toyama.ac.jp; tsubaki@eng.u-toyama.ac.jp

Catalysts and reactors are two essential elements of traditional catalytic systems. Catalysts can change reaction pathway, improve reaction efficiency, or selectively produce target chemicals[1–3]. Reactors possess an important function that provides suitable environments for various catalytic reactions. Although the two essential elements have been developed for so many years, their research focuses were distinctly different. The catalyst researches mainly focused on preparation methods, reaction mechanisms, structure characterizations, catalyst performances, and so on[1,2]. However, the reactor researches were devoted to updating reactor types and functions, enhancing heat and mass transfer, lowering pressure drop, etc.[3] Until now, the researches of catalysts and reactors are still two different directions. Few studies have succeeded in functional integration of catalyst and reactor to effectively control chemical reaction. Therefore, there is a great need to develop their functional integration and synergies for future catalytic systems to realize superior chemical synthesis.

Three-dimensional (3D) printing has been widely studied in biotechnology, prosthetics, architecture, pharmaceutical synthesis, etc. (Fig. 1a)[4–14]. Recently, several research groups have also made considerable progress in catalyst preparation and reactor design[7,8,14–30]. The 3D printing techniques, such as direct ink writing (DIW)[15–24,28], fused deposition modeling (FDM)[14,16,26–28], stereolithography (SLA)[29] and selective laser sintering (SLS)[30], were employed and developed to print the functional catalysts or reactors. The printed catalysts or reactors have exhibited many new and exciting trends for chemical synthesis and analysis. However, the manufacturing principles of the catalysts and reactors were independent of each other. The synergies between them were also overlooked. In addition, the catalysts and reactors were printed separately. It could result in complicated printing process and low printing speed. In view of these problems, it is necessary to explore simple and fast manufacturing strategies. Metal 3D printing reactor, simultaneously coupled with catalytic function, is a feasible approach to overcome these obstacles. Moreover, it can be applied to harsh reaction conditions, such as high temperature and/or high pressure, as in huge catalytic facilities of petrochemical or C1 chemical complex.

Traditionally, petroleum refining is the main way to produce liquid fuel. But, with rapid depletion of petroleum reserves, it is urgent to develop new synthetic routes for conversion of non-petroleum resources (such as natural gas/shale gas, CO_2, biomass) into liquid fuel[31,32]. Fischer–Tropsch (FT) synthesis[33,34], CO_2 hydrogenation[35,36], and CO_2 reforming of CH_4 (DRM)[37,38], as the alternative routes or key steps, have been studied for a long time. But huge operating costs in the conventional plants always prevented them from large-scale industrial applications[39,40]. To effectively reduce the operating costs, metal 3D printing is a very promising technology to revolutionize the devices. On this basis, our integrated design, that is the printed self-catalytic reactors (SCRs) in combination with various catalytic functions (Fig. 1a, b), can further minimize the costs and reactor sizes dramatically, and improve the energy efficiency.

Herein, we design and manufacture three kinds of SCRs (Fe-SCR, Co-SCR, and Ni-SCR) to realize direct conversion of C1 molecules (including CO, CO_2, and CH_4) into high value-added chemicals. The Fe-SCR and Co-SCR produce highly selective synthesis of liquid fuel in high-pressure FT synthesis and CO_2 hydrogenation. The Ni-SCR generates high conversions of CO_2 and CH_4 in high-temperature DRM. Moreover, geometrical studies of the Co-SCRs demonstrate that metal 3D printing itself can enhance synergies between catalyst and reactor, and establish multiple control functions to tune the catalytic product distribution. We anticipate that these printing designs will facilitate the further development of 3D printing technology, and spark a technological revolution of traditional chemical industries and machinery manufacturing industries.

Results and discussion

Catalytic performance of SCRs. Computer-assisted design (CAD, Rhinoceros 5.0) was utilized to create the virtual models of SCRs. To boost up the inner surface area, we designed a series of internal channels and semispherical bulges in the SCRs (Supplementary Fig. 1). The Fe-SCR, Co-SCR, and Ni-SCR were fabricated via SLS technology in the printing processes. Schematic diagram of the SLS technology was displayed in Supplementary
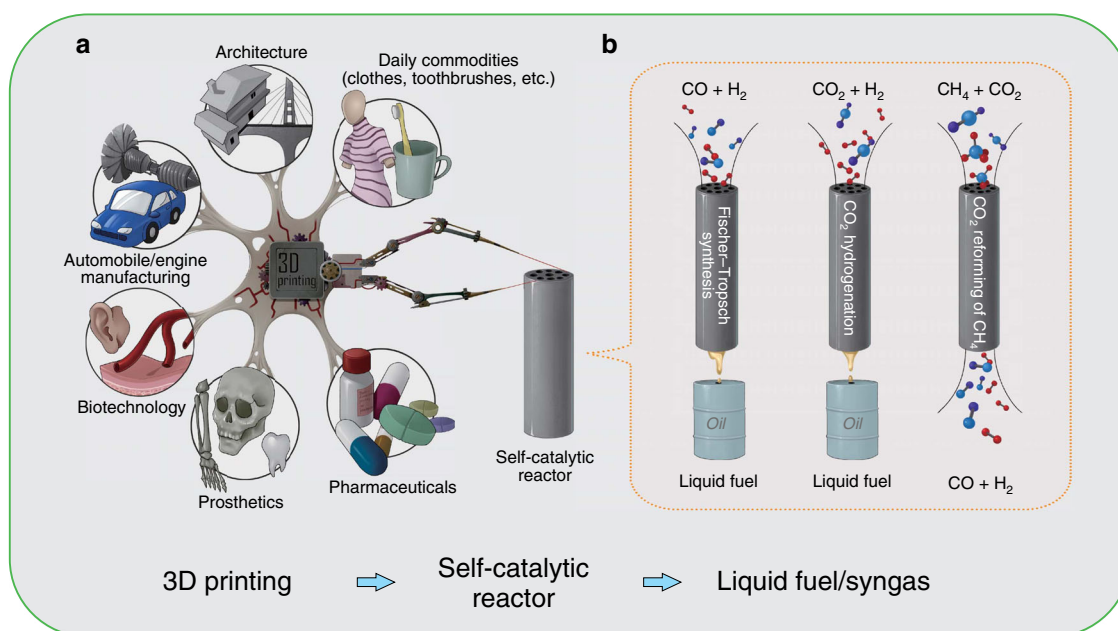

Fig. 1 3D printing for self-catalytic reactor (SCR) and other typical applications. a 3D printing for SCR and other typical applications. **b** The SCR for Fischer–Tropsch (FT) synthesis, CO_2 hydrogenation, and CO_2 reforming of CH_4 (DRM).
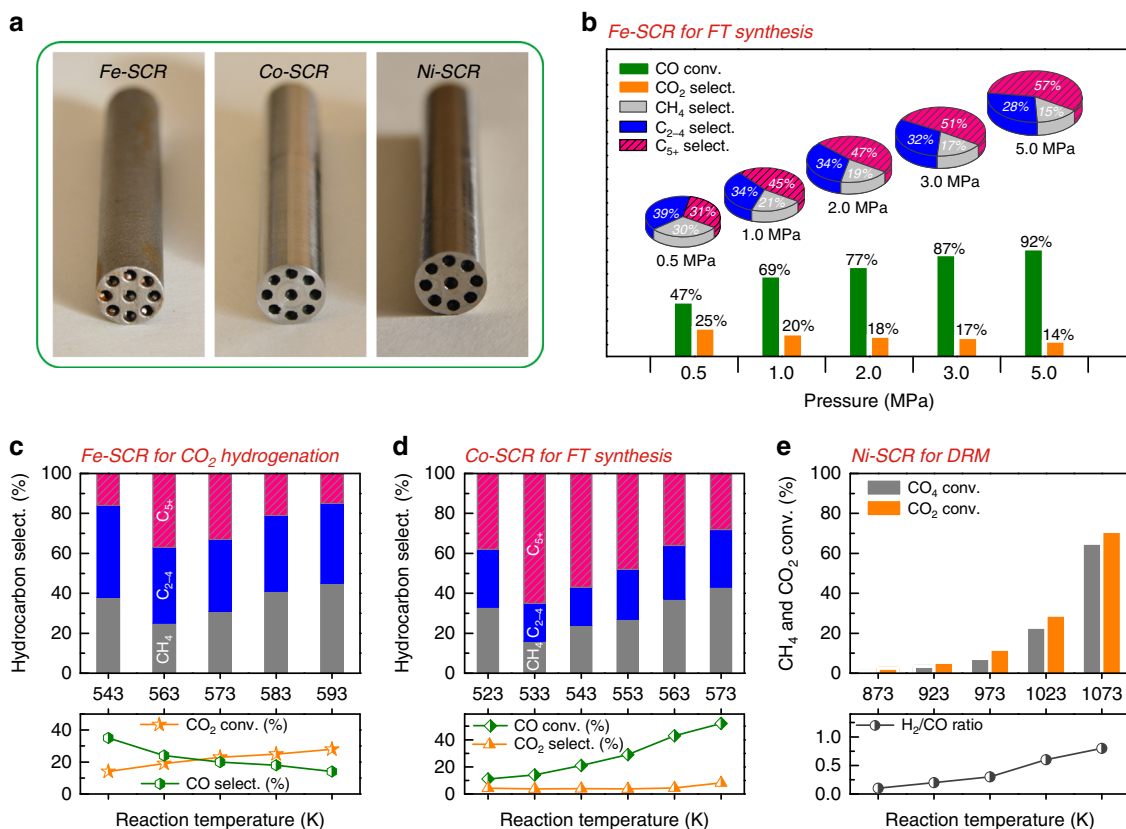
Fig. 2 Catalytic performance of SCRs. a The physical SCRs after polishing the outer surface. **b** Fe-SCR for Fischer–Tropsch synthesis. Reaction conditions: $T = 573$ K; $H_2/CO = 2.0$; flow rate, 20 ml min^{-1}; time on stream, 10 h. **c** Fe-SCR for CO_2 hydrogenation. Reaction conditions: $P = 1.0$ MPa; $H_2/CO_2 = 3.0$; flow rate, 20 ml min^{-1}; time on stream, 10 h. **d** Co-SCR for Fischer–Tropsch synthesis. Reaction conditions: $P = 2.0$ MPa; $H_2/CO = 2.0$; flow rate, 20 ml min^{-1}; time on stream, 10 h. **e**, Ni-SCR for CO_2 reforming of CH_4. Reaction conditions: $P = 0.1$ MPa; $CO_2/CH_4/Ar = 45/45/10$; flow rate, 40 ml min^{-1}; time on stream, 8 h.

Fig. 2. The printing processes were further shown in Supplementary Movie 1 (see Methods for more printing details). Although the printing feedstocks of Fe-, Co- and Ni-based alloy powders (denoted as Fe-, Co-, and Ni-Powder) possessed remarkably different elemental compositions (see Supplementary Tables 1–3), the resulting SCRs still showed the same color and high fidelity (Fig. 2a).

To evaluate the catalytic ability, we first employed the Fe-SCR in FT synthesis. Before the reaction, the Fe-SCR was simply calcined in air and reduced by hydrogen. The obtained samples were denoted as Fe-SCR-*Calcined* and Fe-SCR-*Reduced*, respectively. Fe-Powder, as an allotropic catalyst, was also pretreated using the same calcination and reduction processes. We labeled the resulting samples with Fe-Powder-*Calcined* and Fe-Powder-*Reduced*, respectively. The nitrogen (N_2) physisorption results demonstrated that these pretreatment processes did not significantly change BET areas for the Fe-SCRs or Fe-Powders (Supplementary Table 4). The Fe-SCRs generated low BET areas, because bulk phase of the Fe-SCRs was highly dense and did not contribute to the N_2 physisorption. Traditional reaction tube (T_{316}) was purchased from the Swagelok Company. The T_{316} and the Fe-Powder were also evaluated in FT synthesis. The schematic of FT reaction devices was displayed in Supplementary Fig. 3 and the reaction results were compared in Supplementary Table 5.

The T_{316}, produced by subtractive manufacturing, did not show any catalytic ability for the FT synthesis, probably because it was difficult to activate CO molecules on the smooth and dense surface (Supplementary Figs. 4a, b). The Fe-Powder displayed a high CO conversion of 74%, but the undesired CH_4 and C_{2-4} were the main products. Note that the Fe-SCR also exhibited high CO

conversion. Moreover, the Fe-SCR possessed a higher liquid fuel selectivity of C_{5+} than that of the Fe-Powder. In addition, we also compared linear velocity (V_{linear}) of syngas for the T_{316}, Fe-Powder and Fe-SCR (Supplementary Table 6). The linear velocity (V_{linear}) is defined as translational velocity of syngas, i.e., $V_{linear} = F_{CO+H2} / S_{cat}$. ($F_{CO+H2}$ and S_{cat} represent flow rate of syngas and catalyst surface, respectively). The results unveiled that both the Fe-Powder and the Fe-SCR exhibited lower V_{linear} than the traditional reaction tube T_{316}.

Different from subtractive manufacturing principle, metal 3D printing technology produces the SCRs via a layer-by-layer way, as shown in the Supplementary Movie 1. Thus, high-pressure tolerance of the SCRs is an important checkpoint. Based on this consideration, we dramatically raised the pressure from 0.5 to 5 MPa in FT synthesis (Fig. 2b). Nonetheless, our Fe-SCR system still worked well. The FT results exhibited that the increasing pressures enhanced the CO conversion and C_{5+} selectivity, and inhibited the undesired formation of CH_4, C_{2-4} and CO_2. To further confirm the reliability, we tuned the reaction temperatures and reused the Fe-SCR for 5 times in the FT synthesis (Supplementary Figs. 5, 6). The test results also suggest that the Fe-SCR possesses a wide range of operating temperature and high reusability.

We applied scanning electron microscope (SEM) to investigate the inner microstructure of the Fe-SCR. The results clearly displayed that the Fe-SCR had a grainy inner surface (Supplementary Fig. 4c, d), and significantly differed from the T_{316}. Since Fe-Powder was the feedstock and allotropic catalyst of the Fe-SCR, we further characterized the Fe-Powder before and after the pretreatments, to elucidate the origin of the catalytic ability. The

SEM observation uncovered that although the surface morphology of Fe-Powder was different from that of Fe-Powder-*Calcined*, the average particle sizes still kept at around 18 μm (Supplementary Fig. 7). More importantly, the X-ray diffraction (XRD) patterns and transmission electron microscopy (TEM) results, on the Fe-Powder and Fe-Powder-*Calcined*, showed that the phases of iron alloys were mainly transformed into α-Fe_2O_3 and Fe_3O_4 via the calcination process (Supplementary Figs. 8–12). Their ^{57}Fe Mössbauer spectra and Raman spectra analyses also demonstrated that the α-Fe_2O_3 and Fe_3O_4 were the main phases after the calcination (Supplementary Figs. 13–15 and Supplementary Table 7)[41–46]. According to these analyses of the allotropic catalyst, we consider that the grainy inner surface of the Fe-SCR with the abundant iron oxide species is critical to subsequent FT synthesis.

We also compared the chemical properties of Fe-SCR and Fe-Powder after the pretreatments, to reveal the influence of SLS process on the Fe-SCR. The XRD patterns of Fe-SCR and Fe-SCR-*Calcined*, showed that the iron alloy phases were also transformed into α-Fe_2O_3 and Fe_3O_4 (Supplementary Fig. 16). Although the intensities of XRD peaks were very week, they still displayed the same iron phases as the Fe-Powder and Fe-Powder-*Calcined*, respectively (Supplementary Fig. 8). The energy dispersive X-ray spectroscopy (EDS) analyses further unveiled that the element distributions of Fe-SCR and Fe-SCR-*Calcined* were similar to those of Fe-Powder and Fe-Powder-*Calcined*, respectively (Supplementary Table 8). Moreover, the X-ray photoelectron spectroscopy (XPS) analyses of Fe 2p region, demonstrated that the Fe-SCR and Fe-Powder after the pretreatments also possessed similar surface chemical states of the iron species (Supplementary Fig. 17a, b)[47–50]. Based on these analyses, we confirm that the SLS process of Fe-SCR did not obviously affect their surface chemical properties.

Through the calcination process and FT synthesis, the Fe-SCR changed the color from silver to black (Supplementary Fig. 18a). Because it was difficult to directly characterize the spent Fe-SCR (Fe-SCR-*Spent*) by XRD and ^{57}Fe Mössbauer spectra, we utilized the spent Fe-Powder (Fe-Powder-*Spent*) as a reference sample in the characterizations. The XRD and ^{57}Fe Mössbauer spectra results demonstrated that large part of the iron oxide was further transformed into χ-Fe_5C_2 over the Fe-Powder-*Spent* (Supplementary Figs. 19 and 20 and Supplementary Table 7), which is a well-recognized catalytic center for FT synthesis[50–52]. This observation implies that highly active catalytic center can be readily formed in the Fe-SCR.

To further investigate the highly active iron carbide, we cut the Fe-SCR and Fe-SCR-*Spent* into small slices (Supplementary Fig. 18b), and analyzed cross-section of the slices. The SEM analyses showed that the cross-section of Fe-SCR was monolithic, but a new layer on the inner surface of Fe-SCR-*Spent* was formed (Supplementary Fig. 21a, c). The EDS results demonstrated that the new layer possessed much higher carbon content than bulk phase of Fe-SCR-*Spent* and the cross-section of Fe-SCR (Supplementary Fig. 21b, d). It indicates that the new layer was carburized by FT process. We further employed temperature-programmed oxidation technique (O_2-TPO) to measure the carbon content on the Fe-SCR and Fe-SCR-*Spent*[53,54]. As in Supplementary Fig. 22, the peak I and peak II in the O_2-TPO profiles should be due to inherent carbon species and newly formed carbon species, respectively. According to the O_2-TPO profiles, we calculated the carbon content for the Fe-SCR-*Spent*. The results manifested that the total carbon content was 0.03 wt% of the Fe-SCR-*Spent*, and the carbon retention was 0.14 wt% of the carbon source of syngas (Supplementary Table 9).

We also utilized the XPS analysis to characterize the inner surface of the Fe-SCR-*Reduced* and Fe-SCR-*Spent*. The Fe 2p peaks at 706.8 and 707.2 eV were identified on the Fe-SCR-*Reduced* and Fe-SCR-*Spent* (Supplementary Fig. 17b, c), and were attributed to iron metal and iron carbide[48–50], respectively. This proved that iron metal species were transformed into iron carbide species on the inner surface of Fe-SCR during the FT synthesis. The same phenomena were also observed on the Fe-Powder-*Reduced* and Fe-Powder-*Spent* in the XPS analysis (Supplementary Fig. 17b, c). Moreover, the XRD and ^{57}Fe Mössbauer spectra results of Fe-Powder-*spent* have demonstrated that the χ-Fe_5C_2 was the main phase during the reaction (Supplementary Figs. 19, 20 and Supplementary Table 7). Therefore, we confirm that the grainy inner surface with the highly active χ-Fe_5C_2 on the Fe-SCR promotes the FT performance.

Unexpectedly, the Fe-SCR also exhibited a good performance for CO_2 hydrogenation to liquid fuel, as shown in Fig. 2c. In the hydrogenation, high CO selectivity but low CO_2 conversion were formed in the low-temperature reaction. It indicates that reverse water-gas shift (RWGS: $CO_2 + H_2 = CO + H_2O$) reaction dominated the hydrogenation process[36,55,56]. In contrast, low CO selectivity but high CO_2 conversion were realized during the high-temperature reaction. This suggests that the generated CO from the RWGS was in situ converted into hydrocarbons via CO hydrogenation[36,55,56]. But high CH_4 selectivity was caused by the excessive high temperature. Consequently, by the reaction at 563 K, we obtained the moderate CO_2 conversion of 19% and high C_{5+} selectivity of 37% over the Fe-SCR.

In addition to the Fe-SCR, we also fabricated the Co-SCR for the FT synthesis (see Supplementary Fig. 23 for inner surface morphology). The results were shown in Fig. 2d. By tuning the reaction temperature, the CO conversion significantly increased from 11 to 52%. The undesirable CO_2 selectivity was about 5%, and much lower than that of the Fe-SCR. Moreover, the C_{5+} selectivity could reach 65 %. The inductively coupled plasma atomic emission spectroscopy (ICP-AES) analysis demonstrated no metal contamination in the liquid fuel (Supplementary Table 10). These findings indicate that the Co-SCR not only enhances the liquid fuel selectivity, but also inhibits the formation of CO_2 by-product. Additionally, we compared the thermal conductivity of the Co-SCR and traditional supports (SiO_2 and Al_2O_3) of FT catalysts. As indicated in Supplementary Table 11, the thermal conductivity of the Co-SCR was 7 W m^{-1} K^{-1}, which was much higher than those of the traditional SiO_2 and Al_2O_3. It suggests that local overheating that leads to deactivation of the traditional FT catalysts, can be significantly reduced on the SCRs system[57,58]. More importantly, the high thermal conductivity can greatly improve energy efficiency for the whole reaction system.

To demonstrate high-temperature tolerance of our SCRs, we evaluated the Ni-SCR in DRM reaction (DRM: $CH_4 + CO_2 = 2CO + 2H_2$), at different reaction temperatures. Because FT synthesis and CO_2 hydrogenation are always performed at a relatively low reaction temperature, but DRM is a typical high-temperature reaction (~1000 K), due to the extremely inert feedstocks (CO_2 and CH_4)[59,60]. The DRM results were shown in Fig. 2e. At a high temperature of 1073 K, the CH_4 and CO_2 conversions as high as 65 and 71% were obtained, respectively. The ratio of H_2/CO was close to the stoichiometric ratio of 1. This observation indicates that the Ni-SCR suppresses the side reactions (RWGS and CH_4 decomposition ($CH_4 = C(s) + 2H_2$))[61,62], and keeps a good balance on the formation of CO and H_2. It also signifies that the Ni-SCR successfully resists the high-temperature reaction environment.

Geometrical studies of Co-SCRs. To reveal high degree of flexibility and freedom for our SCRs designs, we conducted the geometrical studies on the Co-SCR. The Co-SCR was further
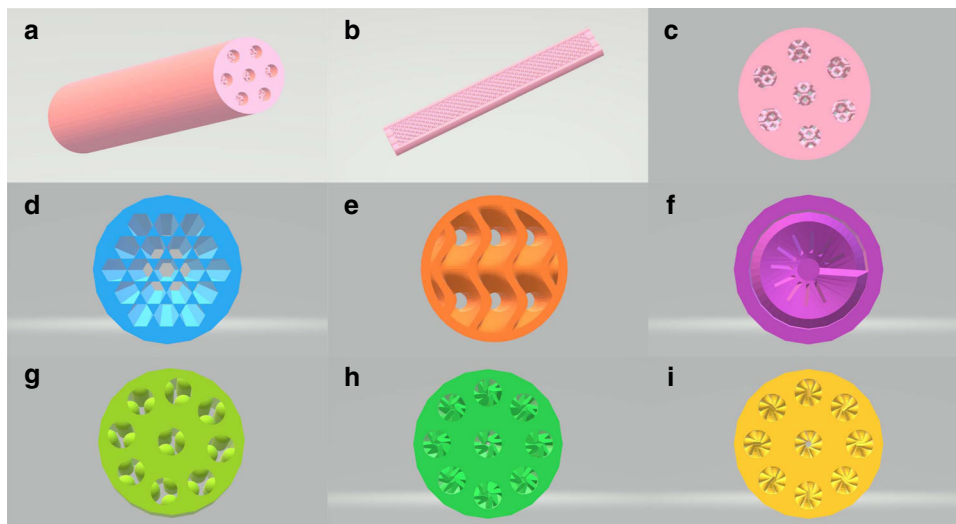
Fig. 3 Geometrical structures of Co-SCRs. (**a**) Co-SCR-1; (**b**) longitudinal section of Co-SCR-1; (**c**) cross-section of Co-SCR-1; (**d**) cross-section of Co-SCR-2; (**e**) cross-section of Co-SCR-3; (**f**) cross-section of Co-SCR-4; (**g**) cross-section of Co-SCR; (**h**) cross-section of Co-SCR-5; (**i**) cross-section of Co-SCR-6.

employed in the studies, due to the fact that it has already exhibited the high liquid fuel selectivity in the FT synthesis. In addition, via using the CAD, we designed the other 6 types of Co-SCRs to tune the inner geometrical structures (denoted as Co-SCRx, $x = 1, 2, 3…,6$; see Fig. 3 and Supplementary Figs. 24, 25). The various morphologies of Co-SCRs were selected in the metal 3D printing, based on the rules of easy realization, tunable geometrical structure, and high tolerance of pressure/temperature. After the printing fabrications, these Co-SCRs were also applied in FT synthesis, to investigate the catalytic performance. We anticipated that the different geometrical designs would optimize the product distribution in the FT synthesis.

The FT results over the seven types of Co-SCRs were summarized, and compared in Fig. 4. Although the Co-SCRs displayed the similar CO conversion, C_{ole}/C_n ratio and C_{iso}/C_n ratio (Fig. 4a), their product selectivities were significantly different. In particular, the C_{5+} selectivity over these Co-SCRs increased from 48 to 73% (Fig. 4b). We also compared the fuel selectivities of gasoline (C_{5-11}), jet fuel (C_{8-16}) and diesel fuel (C_{10-20}), on the Co-SCR-1, Co-SCR-3, and Co-SCR-6 (Fig. 4c). The results exhibited that the Co-SCR-6 generated higher selectivities to the jet fuel and diesel fuel, than the Co-SCR-1 and Co-SCR-3. These findings indicate that these controllable 3D printing structures successfully tune FT product distribution, and increase liquid fuel selectivity. Furthermore, the increase of chain growth probability (α) from 0.57 to 0.86 also suggests that they can promote growth of heavy hydrocarbons, and suppress undesired formation of light hydrocarbons (Fig. 4d)[63,64]. Therefore, we conclude that these tailor-made 3D printing designs can dramatically improve the product distribution, and enhance the catalytic functions.

To obtain the underlying reasons of influencing the liquid fuel selectivity, we further analyzed the inner surface and channel volume, and calculated the liner velocity (V_{linear}) and passage time ($T_{passage}$) of syngas for the Co-SCRs (Supplementary Table 12). The passage time is defined as the time it takes for syngas to pass the channel, i.e., $T_{passage} = V_{channel} / F_{CO+H2}$ ($V_{channel}$ and F_{CO+H2} are the channel volume and flow rate of syngas, respectively). Because the F_{CO+H2} of feed gas was constant in our FT evaluation, the high inner surface and low channel volume of Co-SCRs led to low V_{linear} and $T_{passage}$, respectively.

It is well known in FT synthesis that large catalytic surface area and low linear velocity will enhance re-adsorption of intermediate

α-olefin, to promote new carbon-chain growth[65,66]. Low channel volume and low passage time can reduce secondary reactions (hydrocracking/hydrogenolysis) of long-chain hydrocarbons[33,67], and keep high liquid fuel selectivity in FT process. Moreover, spatial structure of FT reactor plays a key role on regulating the balance between plug-flow and back-mixing modes of reaction gas[68,69]. Therefore, although the Co-SCRs revealed non-linear changes on the inner surface and channel volume (Supplementary Table 12), they still displayed a linear increase on the liquid fuel selectivity (Fig. 4b). It demonstrated that the multiple factors, as mentioned above, worked simultaneously, resulting in the non-linear, overlying phenomena of the factors. These analyses also proved that the SCRs designs can provide three kinds of tunable factors, including inner surface, channel volume and spatial structure, to realize high controllability on chemical synthesis.

In summary, we have successfully designed three kinds of SCRs (Fe-SCR, Co-SCR, and Ni-SCR) via metal 3D printing technology. The C1 catalytic results demonstrated that they can effectively resist the harsh reaction conditions, such as high temperature and high pressure. The Fe-SCR and Co-SCR exhibited excellent performance for FT synthesis and CO_2 hydrogenation to synthesize liquid fuel. The Ni-SCR displayed high conversions and ideal ratio of H_2/CO for CO_2 reforming of CH_4. Further, the geometrical studies of the Co-SCRs clearly revealed that different printing structures can dramatically tune their catalytic functions. This work offers a simple, fast and feasible technology to build functional integration and synergies between reactors and catalysts, and facilitate the new designs of future catalytic system. We expect that this self-catalytic design can stimulate new developments for 3D printing technologies, and wide applications in chemistry, energy, pharmacy, material synthesis, machinery manufacturing, etc.

Methods

Preparation of SCR. The virtual SCRs were created by CAD (Rhinoceros 5.0). The physical SCRs were prepared by metal 3D printing via a SLS. To print Fe-SCR, the Fe alloy powder was first packed in a raw material vat, and the base plate was mounted under the laser source. Then, the Fe alloy powder was rapidly shaped into the physical Fe-SCR on the base plate via transformation of the virtual SCRs. After this process, the residual Fe powder was removed by a vacuum cleaner. The Fe-SCR was obtained by further dismounting the base plate and polishing the outer surface. The fabrication processes of Fe-SCR were conducted by J·3D Co., Ltd. in Japan.

The preparation processes were filmed in Supplementary Movie 1. Via using the same preparation method, we further fabricated Co-SCR and Ni-SCR. To tune the inner surface of the Co-SCR, we applied the CAD to design different structures.
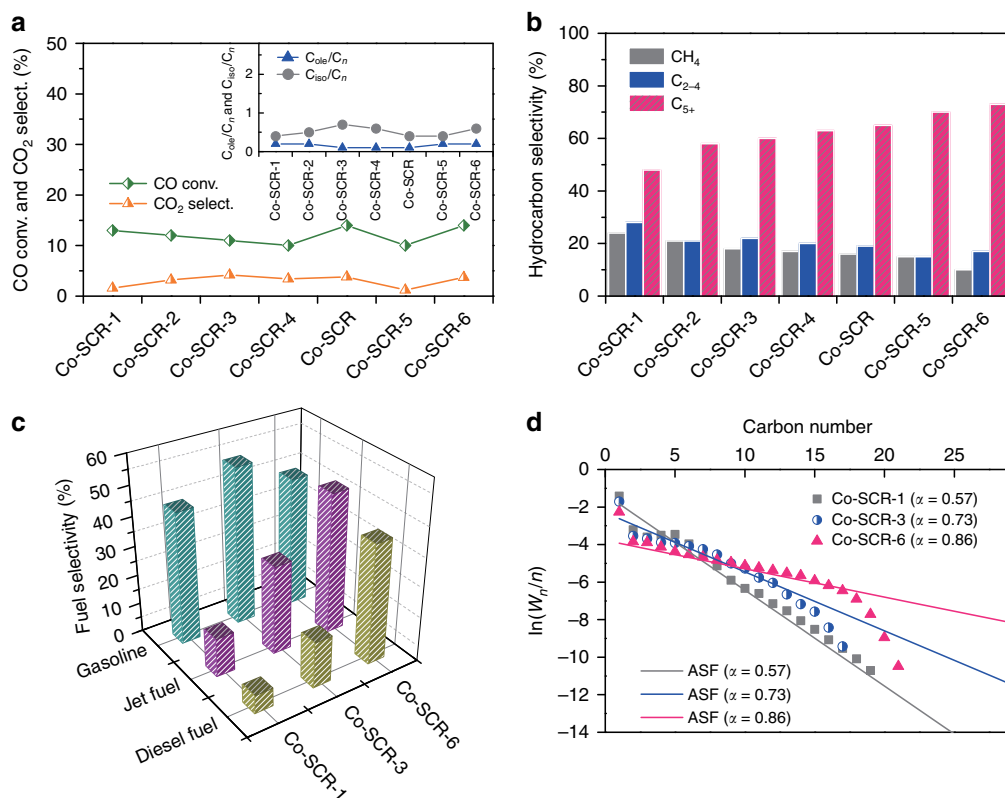
Fig. 4 Impact of geometrical structures on FT product distribution. a CO conversion, C_{ole}/C_n ratio and C_{iso}/C_n ratio of the Co-SCRs. **b** Hydrocarbon distribution of the Co-SCRs. **c** Fuel selectivity of gasoline (C_{5-11}), jet fuel (C_{8-16}), and diesel fuel (C_{10-20}) for the Co-SCR-1, Co-SCR-3, and Co-SCR-6. **d** Chain growth probability (α) of the Co-SCRs. The α value was calculated based on the growth trend of hydrocarbons C_{5-11} over the Co-SCR-1, Co-SCR-3, and Co-SCR-6, respectively. The calculation rule of the α value was according to the Anderson–Schulz–Flory model[63,64]. Reaction conditions: $T = 533$ K; $P = 2.0$ MPa; $H_2/CO = 2.0$; flow rate, 20 ml min^{-1}; time on stream, 10 h.

The other 6 types of Co-SCRs were also obtained using the same printing processes. The fabrication processes of Co-SCR and Ni-SCR were performed by Shanghai Consu Metal Materials Co., Ltd. in China.

To further activate the catalytic centers, the SCRs were simply pretreated before the reactions. The Fe-SCR was calcined in air at 873 K for 60 h, and then reduced by H_2 at 673 K for 10 h with a H_2 flow rate of 40 ml min^{-1}. The Co-SCRs were calcined in air at 1073 K for 24 h, and their inner surfaces were treated by an acid mixture of HCl (8.7 mol l^{-1}) and HNO$_3$ (3.3 mol l^{-1}) with a volume of 160 ml for 2 h. They were also reduced by the same H_2 conditions as those for the Fe-SCR. The Ni-SCR was calcined in air at 873 K for 60 h, and further reduced by H_2 at 1073 K for 6 h with the flow rate of 40 ml min^{-1}. Additionally, traditional reaction tube (T$_{316}$) was prepared from fully annealed and cold drawn stainless steel tube, which was purchased from the Swagelok Company (Type 316 L; Part No: SS-T6-S-049-20). The T$_{316}$ was pretreated by the same procedures as the Fe-SCR. In control experiments, the alloy powder was used as the reference samples and denoted as M (M = Fe, Co, Ni)-Powder. The Fe-Powder was also pretreated by using the same calcination and reduction processes as the Fe-SCR. Finally, these resulting Fe-SCR, Co-SCRs, Ni-SCR, T$_{316}$, and Fe-Powder (0.5 g) were used in C1 catalytic reactions.

Structural characterization. The XRD patterns were conducted on an X-ray diffractometer (RINT 2400; Rigaku) with a Cu-K$_\alpha$ radiation (40 kV and 40 mA). The elemental composition of the alloy powder was determined by a Philips Magix-601 wave-dispersive X-ray fluorescence (XRF) spectrometry. The surface morphology of the alloy powders was obtained by a scanning electron microscopy (SEM; JSM-6360LV; JEOL) with an energy-diffusive X-ray spectroscopy (EDX; JED-2300; JEOL). The transmission electron microscopy (TEM) images and high-resolution transmission electron microscopy images were obtained on a JEM-2100F (JEOL) at an acceleration voltage of 200 kV. The ^{57}Fe Mössbauer spectra at room temperature were recorded on a Topologic 500 A spectrometer with ^{57}Co (Rh) source in a constant acceleration mode. The obtained spectra were fitted using MossWinn 4.0pre program, and the isomer shift values were given relative to α-Fe as the standard. The Raman spectra were carried out on a Renishaw inVia 2000 Raman microscope by using an Ar ion laser at a wavelength of 514.5 nm. The nitrogen physisorption was carried out on a Micromeritics 3Flex surface characterization analyzer. In the analyses, SiO$_2$ pellet was used as an inner standard.

The Fe-SCR samples were cut into small pieces, and then loaded into the physical adsorption analyzer. The X-ray photoelectron spectroscopy (XPS) was performed on a Thermo Fisher Scientific ESCALAB 250Xi instrument with an Al Kα X-ray radiation source. The temperature-programmed oxidation (O$_2$-TPO) was measured on a BELCAT II instrument equipped with an online mass spectrometer (BELMASS, BEL Japan, Inc., Japan). Before the test, the sample of 0.8 g was pretreated with Ar gas (25 ml min^{-1}) at 393 K for 1 h, and then cooled down to 323 K. After a gas mixture of O$_2$/Ar (5 vol.% O$_2$) with a flow rate of 50 ml min^{-1} was introduced into the instrument, the sample was heated to 1173 K with a rate of 10 K min^{-1}. For the quantitative measurement, the TPO profiles were calibrated by measuring a known amount of active carbon under the same conditions. The inductively coupled plasma atomic emission spectroscopy (ICP-AES) was tested using a Thermo Scientific iCAP 6300 instrument.

Evaluation of catalytic performance. FT synthesis was performed on the Fe-SCR and Co-SCRs. The FT apparatus was fabricated by ourselves. After the H_2 pre-treatments, the SCRs were cooled down to 423 K. Syngas with a H_2/CO ratio of 2.0 and flow rate of 20 ml min^{-1} was introduced into the SCRs. Then, the catalytic systems were raised to target temperature and pressure, respectively, to start the reactions. The reusability experiment was conducted on the same reaction conditions. Before the experiment, pretreatments of the spent Fe-SCR were the same those of the fresh Fe-SCR. After the FT synthesis, the gas products were analyzed by two online gas chromatographies (Shimadzu GC-8A with thermal conductivity detector (TCD); Shimadzu GC-14B with flame ionization detector (FID)). The liquid hydrocarbons in the effluent were captured by an ice trap, and analyzed by an off-line gas chromatography (Shimadzu GC-2014 with FID). The hydrocarbon selectivity was calculated based on the C-moles of a product with respect to the total C-moles in the hydrocarbon mixture. The calculation methods for conversion and selectivity are as follows[31,70]:

$$\text{CO conv. \%} = \frac{CO_{in} - CO_{out}}{CO_{in}} \times 100\%, \tag{1}$$

$$\text{CO}_2 \text{ select. \%} = \frac{CO_{2out}}{CO_{in} - CO_{out}} \times 100\%, \tag{2}$$

$$C_n \text{ select. } \% = \frac{nC_n}{\sum_{n=1}^{\max} nC_n} \times 100\%. \tag{3}$$

CO_2 hydrogenation was also conducted on the Fe-SCR. The apparatus was the same with that of the FT synthesis. After the H_2 pretreatments, the Fe-SCR was cooled down to 423 K. Then, the feed gas with a H_2/CO_2 ratio of 3.0 and flow rate of 20 ml min^{-1} was introduced, and the temperature and pressure were increased to the target conditions. The product analyses were similar with those of the FT synthesis. The calculation methods for conversion and selectivity are as follows[35,55]:

$$CO_2 \text{ conv. } \% = \frac{CO_{2in} - CO_{2out}}{CO_{2in}} \times 100\%, \tag{4}$$

$$CO \text{ select. } \% = \frac{CO_{out}}{CO_{2in} - CO_{2out}} \times 100\%, \tag{5}$$

$$C_n \text{ select. } \% = \frac{nC_n}{\sum_{n=1}^{\max} nC_n} \times 100\%. \tag{6}$$

CO_2 reforming of CH_4 was carried out on the Ni-SCR at atmospheric pressure. A gas mixture of CO_2, CH_4 and Ar ($CO_2/CH_4/Ar = 45/45/10$ in vol.%) with a flow rate of 40 ml min^{-1} was employed on this reaction. The reaction effluents were monitored using two online gas chromatographies. The Shimadzu GC-8A with TCD and Porapak Q column was used to analyze the CO, Ar, CH_4, and CO_2; The Shimadzu GC-2014 with TCD and activated carbon column was employed to analyze the H_2. The calculation methods for conversion and H_2/CO ratio are presented as follows[59]:

$$CH_4 \text{ conv. } \% = \frac{CH_{4in} - CH_{4out}}{CH_{4in}} \times 100\%, \tag{7}$$

$$CO_2 \text{ conv. } \% = \frac{CO_{2in} - CO_{2out}}{CO_{2in}} \times 100\%, \tag{8}$$

$$H_2/CO \text{ ratio } = \frac{H_{2out}}{CO_{out}}. \tag{9}$$

Data availability

Source data are provided with this paper. The other data supporting the findings of this study are available from the corresponding authors on reasonable request.

References

1. Ross, J. R. H. *Heterogeneous Catalysis: Fundamentals and Applications* (Elsevier, Amsterdam, 2011).
2. Chorkendorff, I. & Niemantsverdriet, J. W. *Concepts of Modern Catalysis and Kinetics* (Wiley, Weinheim, 2017).
3. Winterbottom, J. M. & King, M. B. *Reactor Design for Chemical Engineers* (Stanley Thornes (Publishers) Ltd., Cheltenham, 1999).
4. Jungst, T. et al. Strategies and molecular design criteria for 3D printable hydrogels. *Chem. Rev.* **116**, 1496–1539 (2016).
5. Ligon, S. C. et al. Polymers for 3D printing and customized additive manufacturing. *Chem. Rev.* **117**, 10212–10290 (2017).
6. Ambrosi, A. & Pumera, M. 3D-printing technologies for electrochemical applications. *Chem. Soc. Rev.* **45**, 2740–2755 (2016).
7. Parra-Cabrera, C. et al. 3D printing in chemical engineering and catalytic technology: structured catalysts, mixers and reactors. *Chem. Soc. Rev.* **47**, 209–230 (2018).
8. Zhou, X. & Liu, C. Three-dimensional printing for catalytic applications: current status and perspectives. *Adv. Funct. Mater.* **27**, 1701134 (2017).
9. Lewandowski, J. J. & Seifi, M. Metal additive manufacturing: a review of mechanical properties. *Annu. Rev. Mater. Res.* **46**, 151–186 (2016).
10. Herzog, D. et al. Additive manufacturing of metals. *Acta Mater.* **117**, 371–392 (2016).
11. Murphy, S. V. & Atala, A. 3D bioprinting of tissues and organs. *Nat. Biotechnol.* **32**, 773–785 (2014).
12. Kang, H. et al. A 3D bioprinting system to produce human-scale tissue constructs with structural integrity. *Nat. Biotechnol.* **34**, 312–322 (2016).
13. Gupta, M. K. et al. 3D printed programmable release capsules. *Nano Lett.* **15**, 5321–5329 (2015).
14. Kitson, P. J. et al. Digitization of multistep organic synthesis in reactionware for on-demand pharmaceuticals. *Science* **359**, 314–319 (2018).
15. Symes, M. D. et al. Integrated 3D-printed reactionware for chemical synthesis and analysis. *Nat. Chem.* **4**, 349–354 (2012).
16. Kitson, P. J. et al. 3D printing of versatile reactionware for chemical synthesis. *Nat. Protoc.* **11**, 920–936 (2016).
17. Zhu, C. et al. Toward digitally controlled catalyst architectures: hierarchical nanoporous gold via 3D printing. *Sci. Adv.* **4**, eaas9459 (2018).
18. Tubío, C. R. et al. 3D printing of a heterogeneous copper-based catalyst. *J. Catal.* **334**, 110–115 (2016).
19. Quintanilla, A. et al. Graphene-based nanostructures as catalysts for wet peroxide oxidation treatments: from nanopowders to 3D printed porous monoliths. *Catal. Today* https://doi.org/10.1016/j.cattod.2019.06.026 (2019).
20. Middelkoop, V. et al. Next frontiers in cleaner synthesis: 3D printed graphene-supported CeZrLa mixed-oxide nanocatalyst for CO_2 utilisation and direct propylene carbonate production. *J. Clean. Prod.* **214**, 606–614 (2019).
21. Magzoub, F. et al. 3D-printed ZSM-5 monoliths with metal dopants for methanol conversion in the presence and absence of carbon dioxide. *Appl. Catal. B* **245**, 486–495 (2019).
22. Middelkoop, V. et al. 3D printed Ni/Al$_2$O$_3$ based catalysts for CO_2 methanation—a comparative and operando XRD-CT study. *J. CO2. Util.* **33**, 478–487 (2019).
23. Díaz-Marta, A. S. et al. Three-dimensional printing in catalysis: combining 3D heterogeneous copper and palladium catalysts for multicatalytic multicomponent reactions. *ACS Catal.* **8**, 392–404 (2018).
24. Azuaje, J. et al. An efficient and recyclable 3D printed α-Al$_2$O$_3$ catalyst for the multicomponent assembly of bioactive heterocycles. *Appl. Catal. A* **530**, 203–210 (2017).
25. Hurt, C. et al. Combining additive manufacturing and catalysis: a review. *Catal. Sci. Technol.* **7**, 3421–3439 (2017).
26. Sangiorgi, A. et al. 3D printing of photocatalytic filters using a biopolymer to immobilize TiO$_2$ nanoparticles. *J. Electrochem. Soc.* **166**, 3239–3248 (2019).
27. Díaz-Marta, A. S. et al. Integrating reactors and catalysts through three-dimensional printing: efficiency and reusability of an impregnated palladium on silica monolith in Sonogashira and Suzuki reactions. *ChemCatChem* **12**, 1762–1771 (2020).
28. Díaz-Marta, A. S. et al. Multicatalysis combining 3D-printed devices and magnetic nanoparticles in one-pot reactions: steps forward in compartmentation and recyclability of catalysts. *ACS Appl. Mater. Interfaces* **11**, 25283–25294 (2019).
29. Manzano, J. S., Wang, H. & Slowing, I. I. High throughput screening of 3d printable resins: adjusting the surface and catalytic properties of multifunctional architectures. *ACS Appl. Polym. Mater.* **1**, 2890–2896 (2019).
30. Lahtinen, E. et al. Fabrication of porous hydrogenation catalysts by a selective laser sintering 3D printing technique. *ACS Omega* **4**, 12012–12017 (2019).
31. Li, J. et al. Integrated tuneable synthesis of liquid fuels via Fischer–Tropsch technology. *Nat. Catal.* **1**, 787–793 (2018).
32. Khodakov, A. Y., Chu, W. & Fongarland, P. Advances in the development of novel cobalt Fischer–Tropsch catalysts for synthesis of long-chain hydrocarbons and clean fuels. *Chem. Rev.* **107**, 1692–1744 (2007).
33. Peng, X. et al. Impact of hydrogenolysis on Fischer–Tropsch synthesis selectivity: diesel fuel production over mesoporous zeolite Y-supported cobalt nanoparticles. *Angew. Chem. Int. Ed.* **54**, 4553–4556 (2015).
34. Zhou, W. et al. New horizon in C1 chemistry: breaking the selectivity limitation in transformation of syngas and hydrogenation of CO_2 into hydrocarbon chemicals and fuels. *Chem. Soc. Rev.* **48**, 3193–3228 (2019).
35. Gao, P. et al. Direct conversion of CO_2 into liquid fuels with high selectivity over a bifunctional catalyst. *Nat. Chem.* **9**, 1019–1024 (2017).
36. Dorner, R. W. et al. Heterogeneous catalytic CO_2 conversion to value-added hydrocarbons. *Energy Environ. Sci.* **3**, 884–890 (2010).
37. Ashcroft, A. T. et al. Partial oxidation of methane to synthesis gas using carbon dioxide. *Nature* **352**, 225–226 (1991).
38. Margossian, T. et al. Molecularly tailored nickel precursor and support yield a stable methane dry reforming catalyst with superior metal utilization. *J. Am. Chem. Soc.* **139**, 6919–6927 (2017).
39. Dry, M. E. The Fischer–Tropsch process: 1950−2000. *Catal. Today* **71**, 227–241 (2002).
40. Shi, L. et al. An introduction of CO_2 conversion by dry reforming with methane and new route of low-temperature methanol synthesis. *Acc. Chem. Res.* **46**, 1838–1847 (2013).
41. Lyubutin, I. S. et al. Mössbauer spectroscopy and magnetic properties of hematite/magnetite nanocomposites. *J. Appl. Phys.* **106**, 034311 (2009).
42. Khollam, Y. B. et al. Microwave hydrothermal preparation of submicron-sized spherical magnetite (Fe$_3$O$_4$) powders. *Mater. Lett.* **56**, 571–577 (2002).
43. Raupp, G. B. & Delgass, W. N. Mössbauer investigation of supported Fe and FeNi catalysts: II. carbides formed Fischer–Tropsch synthesis. *J. Catal.* **58**, 348–360 (1979).

44. Mendili, Y. E. et al. New evidences of in situ laser irradiation effects on γ-Fe₂O₃ nanoparticles: a Raman spectroscopic study. *J. Raman Spectrosc.* **42**, 239–242 (2011).

45. de Faria, D. L., Venâncio Silva, A. S. & de Oliveira, M. T. Raman microspectroscopy of some iron oxides and oxyhydroxides. *J. Raman Spectrosc.* **28**, 873–878 (1997).

46. Shebanova, O. N. & Lazor, P. Raman study of magnetite (Fe₃O₄): laser-induced thermal effects and oxidation. *J. Raman Spectrosc.* **34**, 845–852 (2003).

47. Jia, C.-J. et al. Large-scale synthesis of single-crystalline iron oxide magnetic nanorings. *J. Am. Chem. Soc.* **130**, 16968–16977 (2008).

48. Li, X. & Zhang, W. Sequestration of metal cations with zerovalent iron nanoparticles—a study with high resolution X-ray photoelectron spectroscopy (HR-XPS). *J. Phys. Chem. C.* **111**, 6939–6946 (2007).

49. Butt, J. B. Carbide phases on iron-based Fischer–Tropsch synthesis catalysts part I: characterization studies. *Catal. Lett.* **7**, 61–81 (1990).

50. Yang, C. et al. Fe₅C₂ nanoparticles: a facile bromide-induced synthesis and as an active phase for Fischer–Tropsch synthesis. *J. Am. Chem. Soc.* **134**, 15814–15821 (2012).

51. Santos, V. P. et al. Metal organic framework-mediated synthesis of highly active and stable Fischer–Tropsch catalysts. *Nat. Commun.* **6**, 6451 (2015).

52. Galvis, H. M. T. et al. Supported iron nanoparticles as catalysts for sustainable production of lower olefins. *Science* **335**, 835–838 (2012).

53. Zhang, J. et al. Synthesis of light olefins from CO hydrogenation over Fe–Mn catalysts: effect of carburization pretreatment. *Fuel* **109**, 116–123 (2013).

54. Hamilton, N. G. et al. The application of inelastic neutron scattering to investigate CO hydrogenation over an iron Fischer–Tropsch synthesis catalyst. *J. Catal.* **312**, 221–231 (2014).

55. Wei, J. et al. Directly converting CO₂ into a gasoline fuel. *Nat. Commun.* **8**, 15174 (2017).

56. Wang, W., Wang, S., Ma, X. & Gong, J. Recent advances in catalytic hydrogenation of carbon dioxide. *Chem. Soc. Rev.* **40**, 3703–3727 (2011).

57. Tsakoumis, N. E. et al. Deactivation of cobalt based Fischer–Tropsch catalysts: a review. *Catal. Today* **154**, 162–182 (2010).

58. Tsubaki, N. & Fujimoto, K. Product control in Fischer–Tropsch synthesis. *Fuel Process. Technol.* **62**, 173–186 (2000).

59. Shoji, S. et al. Topologically immobilized catalysis centre for long-term stable carbon dioxide reforming of methane. *Chem. Sci.* **10**, 3701–3705 (2019).

60. Buelens, L. C. et al. Super-dry reforming of methane intensifies CO₂ utilization via Le Chatelier's principle. *Science* **354**, 449–452 (2016).

61. Tomishige, K., Chen, Y. & Fujimoto, K. Studies on carbon deposition in CO₂ reforming of CH₄ over nickel-magnesia solid solution catalysts. *J. Catal.* **181**, 91–103 (1999).

62. Pakhare, D. & Spivey, J. A review of dry (CO₂) reforming of methane over noble metal catalysts. *Chem. Soc. Rev.* **43**, 7813–7837 (2014).

63. Flory, P. J. et al. Molecular size distribution in linear condensation polymers. *J. Am. Chem. Soc.* **58**, 1877–1885 (1936).

64. Friedel, R. A. & Anderson, R. B. Composition of synthetic liquid fuels: I. Product distribution and analysis of C₅-C₈ paraffin isomers from cobalt catalyst. *J. Am. Chem. Soc.* **72**, 1212–1215 (1950).

65. Kuipers, E. W., Vinkenburg, I. H. & Oosterbeek, H. Chain length dependence of α-olefin readsorption in Fischer–Tropsch synthesis. *J. Catal.* **155**, 137–146 (1995).

66. Iglesia, E., Reyes, S. C. & Madon, R. J. Transport-enhanced α-olefin readsorption pathways in Ru-catalyzed hydrocarbon synthesis. *J. Catal.* **129**, 238–256 (1991).

67. Sartipi, S. et al. Catalysis engineering of bifunctional solids for the one-step synthesis of liquid fuels from syngas: a review. *Catal. Sci. Technol.* **4**, 893–907 (2014).

68. Rai, A. et al. Kinetics and computational fluid dynamics study for Fischer–Tropsch synthesis in microchannel and fixed-bed reactors. React. *Chem. Eng.* **3**, 319–332 (2018).

69. Davis, B. H. Fischer–Tropsch synthesis: overview of reactor development and future potentialities. *Top. Catal.* **32**, 143–168 (2005).

70. Zhong, L. et al. Cobalt carbide nanoprisms for direct production of lower olefins from syngas. *Nature* **538**, 84–87 (2016).

Author contributions

Q.W., H.L., and G.L. performed most of the experiments and analyzed the experimental data. Y.H., Y.W., and D.W. conducted the Raman spectroscopy, scanning electron microscopy, and transmission electron microscopy, respectively. Y.E.T. performed the X-ray diffraction. X.P., G.Y., and N.T. designed the research, analyzed the data and wrote the manuscript. All authors discussed the results and commented on the manuscript at all stages.

Competing interests

The authors declare no competing interests.

Additional information

Supplementary information is available for this paper at https://doi.org/10.1038/s41467-020-17941-8.

Correspondence and requests for materials should be addressed to X.P., G.Y. or N.T.

Peer review information *Nature Communications* thanks Juergen Biener, Matti Haukka, Alberto Coelho and the other, anonymous, reviewer(s) for their contribution to the peer review of this work. Peer reviewer reports are available.

Reprints and permission information is available at http://www.nature.com/reprints

Publisher's note Springer Nature remains neutral with regard to jurisdictional claims in published maps and institutional affiliations.